

# Detection of a substructure with adaptive optics integral field spectroscopy of the gravitational lens B1422+231

A. M. Nierenberg<sup>1,2</sup>, T. Treu<sup>1,3</sup>, S. A. Wright<sup>4</sup>, C. D. Fassnacht<sup>5</sup>, M. W. Auger<sup>4</sup>

<sup>1</sup>*Department of Physics, University of California, Santa Barbara, CA 93106, USA*

<sup>2</sup>*amn01@physics.ucsb.edu*

<sup>3</sup>*Packard Fellow*

<sup>4</sup>*Dunlap Institute for Astronomy and Astrophysics, 50 St. George St., Toronto, ON, M5S 3H4, Canada*

<sup>5</sup>*Department of Physics, University of California, Davis, CA 95616, USA*

<sup>6</sup>*Institute of Astronomy, University of Cambridge, Madingley Road, Cambridge, CB30HA, UK*

to be submitted to MNRAS

## ABSTRACT

Strong gravitational lenses can be used to detect low mass subhalos, based on deviations in image fluxes and positions from what can be achieved with a smooth mass distribution. So far, this method has been limited by the small number of suitable (radio-loud) systems which can be analysed for the presence of substructure. Using the gravitational lens B1422+231 as a case study, we demonstrate that adaptive optics integral field spectroscopy can also be used to detect dark substructures. We analyse data obtained with OSIRIS on the Keck Telescope, using a Bayesian method that accounts for uncertainties relating to the point spread function and image positions in the separate exposures. The narrow [OIII] fluxes measured for the lensed images show a significant deviation from what would be expected in a smooth mass distribution, consistent the presence of a perturbing low mass halo. Detailed lens modelling shows that image fluxes and positions are well reproduced by a model with a single subhalo in addition to the main halo. The inferred mass of the subhalo depends on the subhalo mass density profile: the 68 % confidence interval for the perturber mass within 600 pc are:  $8.2^{+0.6}_{-0.8}$ ,  $8.2^{+0.6}_{-1}$  and  $7.6^{+0.3}_{-0.3} \log_{10}[M_{\text{sub}}/M_{\odot}]$  respectively for a singular isothermal sphere, a pseudo-Jaffe, and a NFW mass profile. This method can extend the study of flux ratio anomalies to virtually all quadruply imaged quasars, and therefore offers great potential to improve the determination of the subhalo mass function in the near future.

**Key words:** dark matter – galaxies: dwarf – galaxies: haloes –

## 1 INTRODUCTION

A fundamental prediction of the  $\Lambda$  Cold Dark Matter (ACDM) model is that a Milky Way mass halo should be surrounded by thousands of subhalos. However, only about twenty are observed (e.g. Klypin et al. 1999; Moore et al. 1999; Strigari et al. 2007; Tollerud et al. 2008; Koposov et al. 2008). Significant work in the past decade has gone into understanding this failure in a theory that has otherwise been successful at reproducing the observed power spectrum of structure in the Universe over an enormous range of distance, mass and time scales (e.g. Planck Collaboration et al. 2013; Komatsu et al. 2011).

If CDM is correct, there must be a large number of subhalos which do not retain enough gas (Papastergis et al. 2011) or form enough stars to be detected. A variety of baryonic processes are suspected to lead to dark subhalos. In fact,

star formation in satellite galaxies has been suggested to be quenched by a variety of internal and external process such as UV heating during reionization, tidal and ram-pressure stripping by the central galaxy, supernovae feedback, and stellar winds (e.g. Lu et al. 2012; Menci et al. 2012; Guo et al. 2011; Bullock et al. 2000; Benson et al. 2002; Somerville 2002; Kravtsov et al. 2004; Kaufmann et al. 2008; Macciò 2010; Springel 2010; Zolotov et al. 2012). Significant uncertainty as to the relative importance of various star formation processes remains, with numerous models reproducing the luminosity function of Milky Way satellites while failing to match the satellite luminosity function in different host mass and redshift regimes (Nierenberg et al. 2013). An alternative explanation for the lack of satellites is that dark matter subhalos are not as numerous as predicted by  $\Lambda$ CDM, as in the case of warm dark matter models (Nierenberg et al. 2013).

There are also discrepancies between the subhalo mass profiles predicted by dark matter only CDM simulations and what is observed in Local Group dwarf galaxies. Boylan-Kolchin et al. (2011, 2012), pointed out that the most luminous Milky Way satellites reside in halos which have much lower circular velocities than what is predicted by simulations. Baryonic processes could account for a flattening of the central density profile in the more massive satellite galaxies (Zolotov et al. 2012). Alternatively, self-interacting cold dark matter (SIDM) has been proposed to explain the flattening (e.g. Rocha et al. 2013).

The only way to fundamentally distinguish between these various dark matter models is with a direct measurement of the subhalo mass function which does not rely on an understanding of the baryonic physics in the subhalos. In the Local Group, new work has shown the possibility that dark subhalos may be detected via their interactions with tidal streams (Carlberg et al. 2012), or the HI disk of the Milky Way (Chakrabarti & Blitz 2009). However, these methods are currently limited to low redshifts, and rely on detailed modelling of baryonic structures.

Outside of the low redshift Universe, strong gravitational lensing can be used to measure the subhalo mass function at a range of redshifts, without requiring detailed modelling of baryonic physics. In strong gravitational lensing, a background source is multiply imaged by a foreground deflector, with the image time-delays, positions, and magnifications depending sensitively on the gravitational potential of the deflector, and its first and second derivatives respectively. Precise astrometry and photometry of lensed images have been shown to be powerful ways to measure the mass of low-mass subhalos in proximity to lensed images (e.g. Mao & Schneider 1998; Metcalf & Madau 2001a; Dalal & Kochanek 2002; Koopmans 2005; Amara et al. 2006; McKean et al. 2007; Keeton & Moustakas 2009; MacLeod et al. 2009; Treu 2010; Vegetti et al. 2010b, 2012; Fadely & Keeton 2012).

There are two main requirements for a strong gravitational lens to be suitable for the detection of substructure. First, the background source must be sufficiently large that it is not significantly lensed by stars in the plane of the lens galaxy. For typical lens configurations, stars have Einstein radii of order microarcseconds, thus the background source must be significantly larger than microarcseconds in apparent size. Secondly, the lensed images must contain enough information to constrain the lensing ‘macromodel’, i.e., the smooth mass distribution of the main deflector.

Traditionally, these restrictions have limited the study of substructure to the seven known radio-loud quasar sources which are quadruply imaged (quad). In a seminal work, Dalal & Kochanek (2002) demonstrated that these systems contained a fraction of mass in substructure which was broadly consistent with predictions from CDM simulations, albeit with large uncertainties. Progress with this technique has been limited by the small number of known suitable systems.

An alternative method of using gravitational lensing to study substructure is gravitational imaging proposed by Koopmans (2005) in which subhalos are detected via astrometric perturbations of lensed galaxies. This method has been successfully applied to HST and AO imaging Vegetti et al. (2012, 2010a), and simulations indicate it will also work for ALMA data Hezaveh et al. (2013). The mass sensitivity

of this method is determined by the signal to noise ratio and resolution of imaging, as well as the intrinsic morphology of the lensed galaxy. Current measurements with Keck AO are sensitive to substructure with masses of  $\sim 10^8 M_\odot$  and larger, while measurements with the Next Generation Adaptive Optics on Keck, the Thirty Meter Telescope, Very Long Baseline Interferometry may allow the sensitivity of this method to reach masses of  $\sim 10^6 M_\odot$ .

In this paper we demonstrate for the first time, that subhalos can be detected using strongly lensed *narrow-line* quasar emission, as originally proposed by Moustakas & Metcalf (2003). With this technique, we use spatially resolved spectroscopy in order to measure the flux of narrow line emission in individual lensed images. Quasar narrow-line emission at low redshift is observed to be typically extended over tens to hundreds of parsecs depending on the source luminosity (Bennert et al. 2002), which corresponds to milliarcseconds for typical source redshifts, well above the microlensing scale. A benefit to studying narrow-line emission is that many more quasars have detectable narrow-line emission as opposed to radio emission. This makes this method ideal for measuring the subhalo mass function in the thousands of quad quasar lenses which are expected to be discovered based on their optical properties in ongoing and future surveys including PANSTARRS, DES and LSST (Oguri & Marshall 2010).

While promising, spatially resolved spectroscopy of narrow line emission of quasar lenses has proven difficult to attain. Sluse et al. (2012b) and Guerras et al. (2013) have measured lensed image spectra for pairs of quasar images, and for wide image separation double lenses, and observed differential lensing between the broad and continuum emission, which is evidence for microlensing. In order to study the lensing signal of substructure as discussed before, it is necessary to measure the spectra of images individually. Metcalf et al. (2004) and (Keeton et al. 2006), achieved sufficient spatial resolution in order to measure the broad emission in individual quad quasar images, but neither of these studies detected narrow emission with sufficient signal to noise ratio.

In this paper we present a measurement of narrow-line lensing with unprecedented accuracy using the OH Suppressing Infra-Red Imaging Spectrograph (Larkin et al. 2006, (OSIRIS)) with laser guide star adaptive optics (LGS-AO) (Wizinowich et al. 2006) at Keck. We choose as initial case study the famous system B1422+231 (Patnaik et al. 1992). Previous extensively studies across many bands of photometry (including radio) enable us to compare our measurement with more traditional methods.

The structure of the paper is as follows: In §2 we present our observations. In §3 we describe our Bayesian method for combining multiple exposures to get sub-pixel sampling of the images and extract spectra optimally. In §4 we present the extracted spectra and show fits to the broad and narrow line components in each of the lensed images, and the inferred fluxes from each. In §5 we discuss the gravitational lens models we use to fit the observed image fluxes and positions. In §6 we present results from a gravitational lens model assuming a single perturbing subhalo. In §7 we discuss future prospects for this method. Finally in §8, we summarise our results. Throughout this paper, we assume a flat  $\Lambda$ CDM cosmology with  $h = 0.7$  and  $\Omega_m = 0.3$ . All magni-

tudes are given in the AB system (Oke 1974) unless otherwise stated.

## 2 OBSERVATIONS

We observed the gravitationally lensed quasar B1422+231 on June 10 2012 at the W. M. Keck 10 m telescopes, using OSIRIS with LGS-AO corrections. To maximise the signal-to-noise ratio we used the largest available pixel scale which is  $0''.1$ . We used broad-band K ( $\lambda = 2.17$  microns) filter which provided a spatial field of view of  $\sim 1''.6 \times 6''.4$  and a spectral range of 416 nm in the observed frame. At the time of our observations, the instrument had recently been moved and the full calibration had not yet been performed. As a result we were limited to a bigger wavelength range and smaller field of view that made it possible to only fit three of the four images in the field of view. We observed the system using 300 s exposures, dithering along the long axis of the field of view, with sub-pixel offsets in order to recover more spatial information, for a total of 2700 s of integration. We used the OSIRIS data reduction pipeline to turn the raw CCD images from each exposure into rectified, telluric corrected, and sky emission-subtracted data ‘cubes’ in which the spatial information of the images appeared in the x-y plane of the images, and the wavelength varied along the third dimension.

## 3 DATA REDUCTION

Our goal is to measure integrated line fluxes separately for each lensed image, taking into account all uncertainties regarding image positions, image deblending and PSF properties. We do this in a three step process.

First, we infer the properties of the PSF and image positions in ‘white’ images, which we created by taking the variance-weighted mean of the data cube over the wavelength region dominated by the broad and narrow line emission between rest frame 4700 - 5100 Å. These white images are effectively narrow band images of the system. Figure 1 shows the white image for a single exposure.

Next, we use a Bayesian inference in order to model the system as three point sources (e.g., the three observed lensed-QSO images). The model contains a set of global parameters that are the same for all exposures (the offsets between the three sources and their relative fluxes) and a set of parameters that vary from exposure to exposure (the sky level, the absolute location of the images, the total flux of the three images, and properties describing the shape of the PSF for each exposure). The PSF is modelled as two concentric Gaussians to represent the seeing halo and the AO corrected diffraction core. The inner diffraction core is fixed to be circular and to have a full width at half maximum (FWHM) of  $0''.065$ , based on the size of the telescope and the wavelength of observation (see also van Dam et al. 2006). The seeing halo Gaussian FWHM, ellipticity, position angle, and amplitude relative to the diffraction core Gaussian are free parameters. We run an Markov Chain Monte Carlo (MCMC) sampler for at least ten thousand steps in order to explore the full posterior probability distribution function, including degeneracies between the parameters. We tested

this method by simulating images with the same image separations and signal-to-noise ratio as our data set, and found that we could recover the image positions to an accuracy of better than 5 mas, and the image fluxes to percent level accuracy.

The resulting measured image positions are given in Table 1. Note that these are rotated slightly with respect to the HST images. Our observations occurred during excellent conditions, with typical Strehl  $\sim 0.2-0.3$ , and seeing of  $\sim 0''.3$

Finally, we extract the spectra using the inferred PSF properties and image positions, relying on the fact that the PSF does not vary significantly over the short wavelength range we are considering ( $\sim 180$  nm observed). We draw sets of parameters describing the PSF and image positions from the MCMC chains obtained in the previous step. Then, for each set of parameters, for each wavelength slice in the data cube, we perform a  $\chi$ -squared optimisation via linear inversion in order to find the best fit amplitudes for the lensed images simultaneously for all exposures, allowing for variations in the background flux as a function of wavelength and exposure. The final extracted spectrum for each image is then given by the mean and standard deviation of the best fit image fluxes in each wavelength slice after iterating over all of the parameter draws. This method allows us to quickly and robustly incorporate uncertainties in our inference of the image positions and PSF parameters directly into our spectral extraction. Image spectra are plotted in Figure 1.

## 4 INTEGRATED LINE FLUXES

Having extracted spectra for each of the lensed images, the next step in our analysis is to measure the integrated line fluxes by modelling the spectra as a sum of narrow H- $\beta$  and [OIII], broad H- $\beta$  and continuum emission<sup>1</sup>.

Our data give us three independent measurements of the quasar spectrum, which we expect to be magnified relative to each other due to gravitational lensing. We model the broad H- $\beta$  emission and narrow emission lines as being composed as linear sums of 5th and 3rd order Gauss Hermite polynomials respectively, while the continuum is modelled as a power law. The model imposes the same narrow line FWHM and centroid for all 3 lensed QSO images. The broad and narrow emission lines are allowed to be redshifted relative to each other to account for winds.

The amplitudes of the continuum, narrow, and broad emission lines are all free to vary between the lensed images. The broad line width and continuum slope are also inferred separately for each spectra to account for the differential effects of microlensing and intrinsic variability, which will more strongly lens the continuum and high-velocity tails of the broad emission line as these are emitted from the smallest physical area. Figure 2 shows an example of the decomposition of the spectrum into the four components for image B. Uncertainties in the decomposition are incorporated into the final calculated line fluxes by drawing 1000 random samples from the posterior probability distribution of the spectral parameters and re-computing the line fluxes for each

<sup>1</sup> We also tested for the presence of broad iron nuclear emission, but did not find a significant contribution, and thus omitted it from the final analysis.

| Component | dRa                | dDec               | [OIII] flux       | broad H- $\beta$ | continuum      |
|-----------|--------------------|--------------------|-------------------|------------------|----------------|
| A         | $0.387 \pm 0.005$  | $0.315 \pm 0.005$  | $0.88 \pm 0.01$   | $4.67 \pm 0.06$  | $46.3 \pm 0.1$ |
| B         | $0 \pm 0.005$      | $0 \pm 0.005$      | $1.00 \pm 0.01$   | $5.2 \pm 0.1$    | $44.6 \pm 0.1$ |
| C         | $-0.362 \pm 0.005$ | $-0.728 \pm 0.005$ | $0.474 \pm 0.006$ | $2.5 \pm 0.1$    | $24.1 \pm 1$   |
| D         | $0.941 \pm 0.01$   | $-0.797 \pm 0.01$  | -                 | -                | -              |
| G         | $0.734 \pm 0.01$   | $-0.649 \pm 0.01$  | -                 | -                | -              |

**Table 1.** Image positions and fluxes for images A B and C measured with OSIRIS. Fluxes are in units of the [OIII] flux of image B which was measured to be  $1.4 \pm 0.2 \times 10^{-14} \text{erg}/(\text{s cm}^2)$  by Murayama et al. (1999). Distances are in units of arcseconds. The position for image D comes from averaging the offsets from radio observations by Patnaik et al. (1999) (see Equation 1), while the position for the main lens galaxy (G) comes from averaging the offsets from HST observations from the CASTLES website.

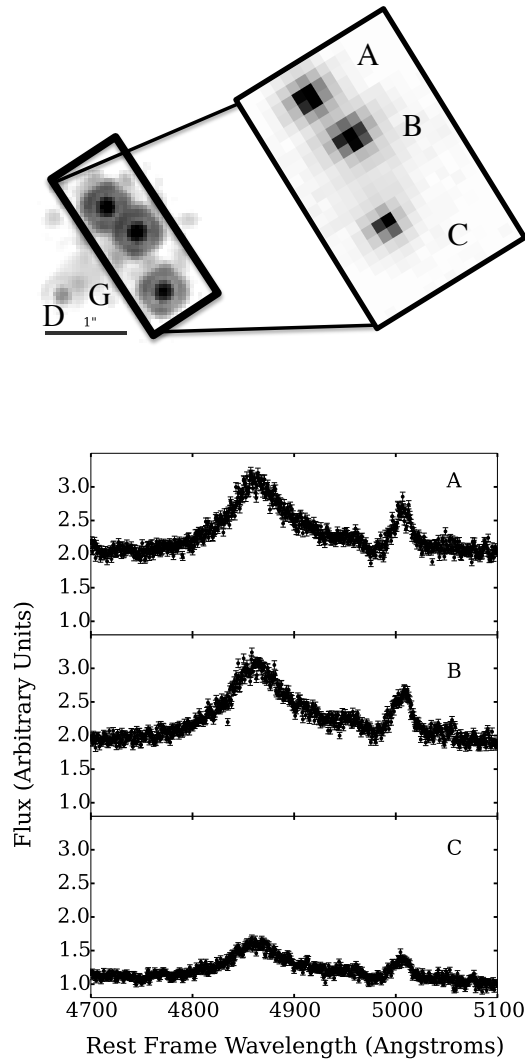


**Figure 1.** Upper Left: HST NICMOS F160W image. Upper Right: Single 300s K band exposure of target using OSIRIS with adaptive optics at Keck, we were restricted to the small field of view due to instrument difficulties. Lower panels: The final extracted spectra for each of the images.

sample draw. The integrated line fluxes with measurement uncertainties for each image are given in Table 1.

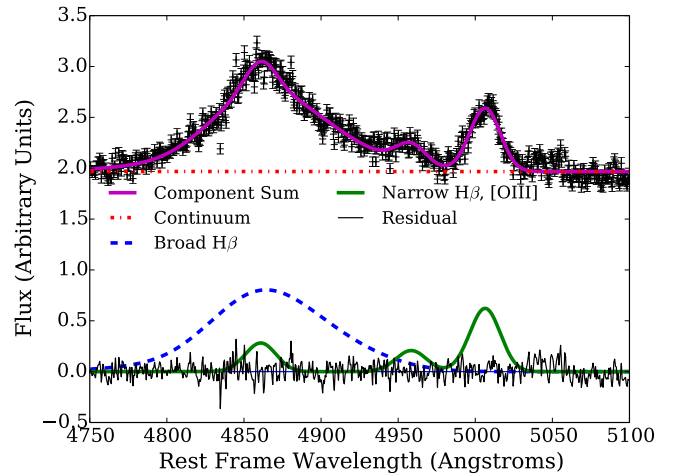


**Figure 2.** Demonstration of best fitting model spectrum to the spectrum of image B, as well as each of the separate line components.

#### 4.1 Astrometry of image D and the main lens galaxy

Although our measurement with OSIRIS only contains information for image fluxes and positions for three of the four images of the system, we incorporate information on the position of the fourth image from previous radio imaging by Patnaik et al. (1999). The position of the fourth image aids in the constraint of the model for the main deflector, and is not expected to vary relative to the other images over time. We take the position of image D to be the mean position after applying the offsets measured by Patnaik et al. (1999) between the three measured image positions:

$$\mathbf{x}_D = 1/3 \sum_{i=A,B,C} \mathbf{x}_i - (\mathbf{x}_{i,p} - \mathbf{x}_{D,p}), \quad (1)$$

where  $\mathbf{x}_{p,i}$  represents position measurements of the  $i^{\text{th}}$  image by Patnaik et al. (1999), and  $\mathbf{x}_i$  is the corresponding measurement in this work. The uncertainty in position D is the standard deviation of the positions. The flux of image D is not used as a constraint in the lens modelling.

Similarly, we use the relative position of the lens galaxy in HST imaging from the CfA-Arizona Space Telescope

LEns Survey (CASTLES) website<sup>2</sup> in order to constrain the centroid of the main deflector in the lens model.

## 5 GRAVITATIONAL LENS MODELLING

Having obtained the integrated narrow-line fluxes and image positions, we can now test for the presence of substructure in the system using gravitational lens modelling. As noted in the introduction, the positions and fluxes of the lensed narrow-line emission images are determined by the first and second derivatives respectively of the gravitational potential of the deflector, and therefore can be used to recover the mass distribution of the perturber as well as the main deflector.

We begin in Subsection 5.1 by modelling the lens as containing a single main deflector with no substructure in an external shear field, and find the best fit mass model parameters given our image fluxes and positions using `gravlens` by Keeton (2001b,a). As with previous studies, we find that this mass model provides a poor fit to the image fluxes. In Subsection 5.2, we explore the effects of adding a single perturber to the system with varying mass profiles.

### 5.1 Singular Isothermal Ellipsoid Deflector

Following numerous previous studies, we model the deflector as a singular isothermal ellipsoid (SIE) which has been shown to provide a good fit to the macroscopic mass distribution of lens galaxies (Treu 2010). The SIE has a density distribution given by:

$$\rho(r) = \frac{\rho_o}{r^2} = \frac{\sigma_v^2}{2\pi r^2 G} = \frac{b}{2\pi r^2} \left( \frac{c^2}{4\pi G} \frac{D_S}{D_{LS} D_L} \right) \quad (2)$$

Where  $\sigma_v$  is a velocity dispersion,  $b$  is the Einstein radius of the lens, and  $D_S$ ,  $D_{LS}$  and  $D_L$  are the angular diameter distances from the observer to the source, from the lens to the source and from the observer to the lens respectively. In `gravlens`, the radius is in elliptical coordinates such that:

$$r = \sqrt{x^2(1 - \epsilon) + y^2(1 + \epsilon)}, \quad (3)$$

where  $\epsilon$  is related to the axis ratio  $q$  by  $q^2 = (1 - \epsilon)/(1 + \epsilon)$ . This means that the Einstein radius is defined along the intermediate axis between the major and minor axes.

As is customary, we also allow for the presence of external shear  $\gamma$  in the direction  $\theta_\gamma$  in order to account for the fact that B1422+231 is a member of a group of galaxies (e.g. Kundic et al. 1997).

We determine the lens model parameters by first using the `gravlens` optimisation routine in order to find the maximum likelihood parameters for the central deflector given the observed image positions and narrow-line flux ratios. We then use `emcee hammer` (Foreman-Mackey et al. 2013), which is a Markov Chain Monte Carlo algorithm which is efficient at exploring highly degenerate parameter spaces, in order to determine uncertainties in the parameter values. We initialise the proposal values in a small region in parameter space around the best fit solutions from `gravlens`, and then for each proposed set of host properties, we use `gravlens` in

order to optimise the source position and compute the  $\chi^2$  for the resulting image positions and magnifications.

The inferred median and one sigma uncertainties for the lens model parameters are given in Table 2. The inferred Einstein radius and lens position are consistent with previous studies which used IR and radio data (Mao & Schneider 1998; Keeton 2001c; Bradač et al. 2002; Sluse et al. 2012a). In some cases our inferred host position angle and external shear parameters deviate slightly. This is likely due to the well-known degeneracy between host ellipticity and PA and the direction and strength of external shear. These studies typically do not report uncertainties nor correlations between their parameters, preventing a more detailed investigation of this effect.

The corresponding model prediction for the image fluxes and positions are given in Table 3. The model provides an excellent fit to the image positions, matching them within the measurement uncertainties, however the predicted image flux ratios deviate significantly from the observation, so that the typical model  $\chi^2$  is  $\sim 50$  for three degrees of freedom. The significant deviation between the observed [OIII] image flux and the smooth model prediction is consistent with previous observations of the system across a broad range of wavelengths, which also found that flux of image A is about 20% brighter relative to image B than predicted by the single deflector model. Figure 3 compares the [OIII] flux ratios between images A, B and C with measurements made at other wavelengths, and also relative to the smooth model prediction.

In Figure 3, we also show our measured flux ratios in the continuum and broad H $\beta$  emission. The broad H $\beta$  emission has flux ratios consistent with that of the narrow emission, while the continuum emission deviates more dramatically from the smooth model prediction. This is consistent with microlensing which can act in conjunction with millilensing by a subhalo, and would most strongly affect the smaller continuum source size.

In order to improve the model fit, a natural solution is to add a perturber less massive than the central galaxy. This can alter image fluxes without significantly shifting image positions, because image fluxes depend on the second derivative of the lensing potential, while image positions depend on the first derivative. In the following subsection we explore the effects of adding a single perturbing mass to the lens system.

### 5.2 Smooth model plus Perturber

As can be seen in Figure 3, the ratio between the fluxes of image A and B deviates significantly from the smooth model prediction while the ratio between fluxes of image C and B does not. The simplest solution is that image A has been magnified by a nearby perturber (Mao & Schneider 1998; Dobler & Keeton 2006), with the amount of magnification depending on the perturber position, mass scale and mass profile.

We explore the simple case of adding a single perturber to the SIE plus external shear model. This is a useful way to understand how our astrometric and photometric precision allows us to constrain the presence of substructure, and to compare our results with previous works, who have also assumed a single perturbing subhalo to the smooth lens model.

<sup>2</sup> [www.cfa.harvard.edu/castles/](http://www.cfa.harvard.edu/castles/)

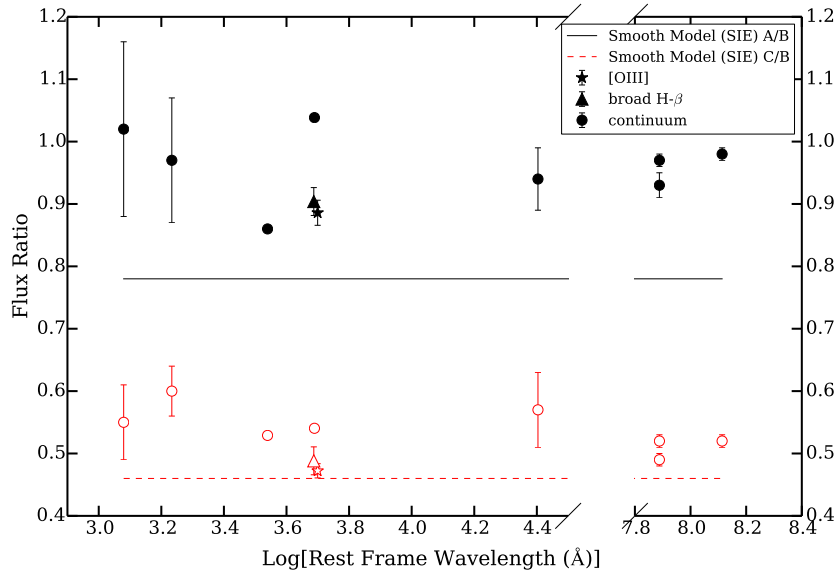


**Figure 3.** Comparison of measured ratios of images A/B and C as a function of wavelength, with the narrow (star), broad (triangles) and continuum measurements in this work. We include HST measurements with WFPC2 F791W and F555W measurements from the CASTLES website, while the NICMOS F160W measurement is from Sluse et al. (2012a). The mid-IR measurement is from Chiba et al. (2005). Radio measurements are from Patnaik et al. (1992, 1999). The solid and dashed lines represent the best-fit prediction to the [OIII] fluxes for the flux ratios between images A/B and C/B respectively, assuming one lens galaxy which is a singular isothermal ellipsoid with external shear. While the ratio between image B and C agrees well with the model, the ratio between A/B is significantly different from the smooth model prediction.

In reality, the system is likely to contain thousands of lower mass subhalos. However the majority of these subhalos will be too low in mass and too far from the lensed images to affect them. The degeneracies between perturber positions and mass make it difficult to distinguish between the effects of populations of perturbers and a single perturber added to the main lens system (Fadely & Keeton 2012). With a larger sample of lens systems, the statistical properties of the perturber population can be inferred more robustly, thus we will leave a more physical model with a realistic population of substructure to a future work in which we consider a larger sample of lensed quasar systems.

For illustrative purposes we consider three mass profiles for the perturber, in order to explore how the mass profile affects the perturber lensing signal. Below we discuss each of the mass profiles in detail.

The simplest mass profile computationally is the singular isothermal sphere (SIS) given by Equation 2, with ellipticity set to zero. This profile is not physical as it diverges as  $r$  goes to zero and extends outward indefinitely, however it provides a good approximation to the small scale density profiles of galaxies (e.g. Gavazzi et al. 2007; Koopmans et al. 2009).

It is expected that a subhalo will undergo truncation by tidal forces from the main halo. This truncation can be modelled by a pseudo-Jaffe profile (PJ, Muñoz et al. 2001), which has a density distribution:

$$\rho(r) = \frac{\rho_o}{r^2} \frac{a^4}{r^2 + a^2}, \quad (4)$$

where  $\rho_o$  is the same as in Equation 2. The truncation radius,  $a$ , is traditionally calculated by assuming that the per-

turber is exactly within the plane of the lens galaxy at the Einstein radius,  $b_{host}$ , so that  $a = \sqrt{b_{sub} b_{host}}$  (Metcalf & Madau 2001b). The SIS and PJ models bracket two extreme cases of no tidal stripping on the one hand, and maximum tidal stripping (in the absence of baryons) on the other.

The third mass profile we consider is the Navarro Frenk and White (Navarro et al. 1996, NFW) profile. This mass profile is predicted by dark matter-only simulations, which may be a better match to the mass profile of subhalos than the SIS profiles. In fact the mass profile of subhalos may be even shallower than this at the centre (e.g. Walker & Peñarrubia 2011; Wolf & Bullock 2012; Hayashi & Chiba 2012), but we leave a more complete exploration of the effects of mass profile variations to a future work. The density distribution of the NFW halo is:

$$\rho(r) = \frac{\rho_s}{(r/r_s)(1+r/r_s)^2} \quad (5)$$

Where  $r_s$  and  $\rho_s$  are the scale radius and the density at the scale radius respectively. To reduce the number of free parameters, we apply the mass-concentration relation predicted by Macciò et al. (2008), assuming a WMAP5 cosmology Dunkley et al. (2009). This is a large extrapolation at dwarf galaxy scales, but allows us to make a useful one-parameter comparison with the steeper mass profiles.

As a first step, we again use **gravlens** to find the best-fit model to the narrow-line fluxes and positions for the macromodel parameters (host and external shear) as well as the perturber mass and position in the case of each of the three perturber mass profiles. As with the SIE only model, we then use **emcee hammer** to infer the model parameters, allowing both the macromodel and the substructure parameters to

vary. For each proposed perturber mass scale, position and set of host properties, we use `gravlens` in order to optimise the source position and compute the  $\chi^2$  for the resulting image positions and magnifications.

As we will demonstrate below, despite the degeneracies, the possible perturber positions are restricted by the proximity of image B to image A, as well as by the critical curve of the main lens. Furthermore, the astrometric precision of the measurement prevents a subhalo large enough to cause significant astrometric deviations from the smooth model. These effects can all be accounted for in the `gravlens` code. We also place lower limits on the mass of the perturber based on the finite size of the source, which we describe below.

### 5.3 Finite Source Effects

The finite nature of the source places lower limit to the perturber mass that can cause the observed magnification (Dobke & King 2006). This can qualitatively be understood by the fact that observed magnification is the convolution of the magnification pattern with the source surface brightness distribution. The larger the source the more small-scale features in the magnification due to low-mass substructure will be smeared out. In the following subsection we discuss how we infer the narrow-line emission source size and use this to place lower limits on the perturber mass for the three different perturber mass profiles.

The observed images in each exposure are a convolution of the PSF in that exposure which we modelled as the sum of two concentric Gaussians in Section 3, with the source which we assumed to be a point source. This was a valid assumption given that the flux in the images between 4500-5100 Å is dominated by continuum and broad H-β emission, which are point-like ( $\mu\text{as}$ ) relative to the resolution of the telescope.

However, this is not the case for [OIII] which is possibly resolved at our resolution. To estimate its size we created an emission line image by subtracting a variance weighted mean image of the continuum region between rest-frame 5070-5140 Å from a variance weighted mean image which contains [OIII] plus continuum between rest frame 4980-5030 Å.

We re-infer the PSF properties using a modification of the analysis described in Section 3. This time, we model the source as an additional Gaussian, which, when convolved with the PSF Gaussians yields observed image widths given by:

$$\sigma_{eff} = \sqrt{\sigma_{PSF}^2 + (\mu^{1/2}\sigma_{source})^2}, \quad (6)$$

where  $\sigma_{PSF}^2$  is the standard deviation of either the seeing-halo or the diffraction core, and  $\mu$  is the best fit magnification given by `gravlens` at each of the image positions.

We find that the [OIII] emission has an intrinsic FWHM of  $\sim 15$  mas. In order our ability to resolve such small sizes, we also model the continuum emission only image, expecting this to be unresolved, even after magnification. We find that the continuum emission has a maximum inferred source size of  $\sim 10$  mas, probably because the core of the PSF is not as narrow as in our model. However, the [OIII] emission is definitely larger and thus resolved. Subtracting the two in quadrature we estimate the intrinsic OIII size to be  $\sim 10$

mas. This corresponds to approximately 60 pc at the redshift of the quasar.

Based on the size-luminosity relation for type one AGN measured in the Local Universe by (Bennert et al. 2002), we would have expected the full narrow-line region in B1422+231 to extend to several hundreds of pc. However, we are likely to only be sensitive to the highest surface brightness parts of the narrow line regions because of surface brightness sensitivity and cosmological dimming. So it is expected that our measurement be smaller than in the local universe. Furthermore, we do not consider lensing shear distortions which are expected to cause the images to be elongated tangentially to the radial direction, rather than simply enlarged isotropically as our analysis assumes. Thus this simple calculation should be considered a lower limit to the true narrow line emission region size, which corresponds to a conservative lower limit to the perturber mass. In other words, a larger narrow line region would result in a more narrow posterior distribution function of the perturber mass.

Dobler & Keeton (2006), computed the relationship between the source size and the minimum Einstein radius of an SIS perturber that can cause the observed magnification of image A, given the convergence and shear of the system B1422+231. They found that an SIS perturber must have mass within the Einstein radius greater than  $b > 0.056a$ , where  $b$  is the Einstein radius of the SIS perturber, and  $a$  is the unlensed source size. This corresponds to a lower mass limit of  $\sim 10^{6.5}$  and  $\sim 10^6 M_\odot$  within 600 pc in the case of the SIS and PJ perturbers respectively, assuming the perturbers are in the plane of the lens galaxy.

The mass limit on the NFW perturber cannot be computed analytically. We approximate this limit by computing the average magnification in a grid of points with a size of the magnified image, for increasing perturber masses. The limit is then given approximately by the minimum perturber mass that can achieve the observed magnification in a region the size of the magnified image. This is an approximate result, as it assumes the source is magnified isotropically rather than distorted as it actually is. In the case of the SIS perturber, for instance, with this method we find that the perturber must be greater than  $b > 0.04a$ , which is slightly lower than the true value computed by Dobler & Keeton (2006), but is good enough for an order of magnitude estimate of the minimum perturber mass. In the case of an NFW perturber with mass concentration relation given by Macciò et al. (2008), the perturber must have a scale radius which is approximately five times larger than the unlensed source size, which corresponds to a mass limit of  $\sim 10^{6.5} M_\odot$  within 600 pc.

## 6 RESULTS

The SIE host plus perturber lens models show significant improvement relative to the SIE only model for all three perturber mass profiles, with best fit  $\chi^2$  of one or smaller for zero degrees of freedom. The model prediction for the image positions and fluxes are listed in Table 3, for the case of an SIE host with an SIS perturber. The perturber does not significantly affect the image positions relative to the smooth model case, while providing a much better fit to the observed

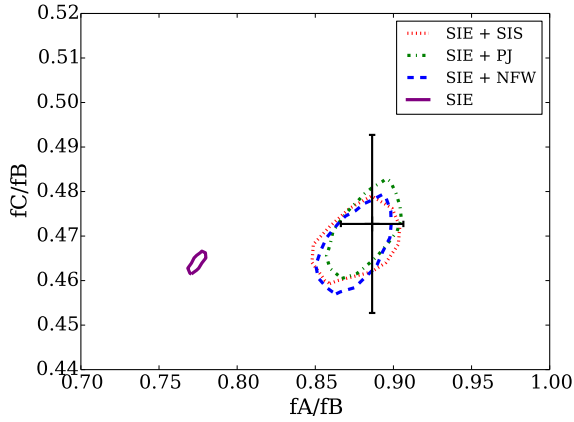


**Figure 4.** Posterior 68% confidence interval for model fluxes for the three host plus perturber models, and the smooth, host only model. The observed flux ratio is given by the black point with error bars. All three perturber models provide significantly better fits to the observation.

flux ratio between images A and B. The improvement in matching the observed flux ratios is equal for all three mass profiles, as can be seen in Figure 4, where we show the one sigma contours for the model predicted flux ratios in the case of the three host plus perturber models as well as the smooth, host only model. These contours are determined relative to the maximum likelihood point in each case.

In Table 2 we list the median and one sigma confidence intervals for the lens model parameters in the case of an SIE host galaxy and an SIS perturber. The host model parameters are consistent with those in the smooth model case, which is expected given the fact that the perturbing halo is a relatively small addition to the mass of the system.

While all three host plus perturber models provide equally good fits to the observations, the posterior probability distributions for the perturber’s position and mass vary significantly as can be seen in Figure 5. There is similar qualitative behaviour in the sense that the further a perturber is from image A, the more massive it must be to achieve the same lensing effect. Furthermore, in all three cases, the mass range is limited naturally by the astrometric precision of the measurement. If the perturber becomes too massive it causes significant astrometric perturbations to the whole system, rather than just affecting the flux of image A. However, the posterior probability distribution for the SIS perturber position is much broader than in the case of the PJ profile due to the fact that the SIS mass profile extends outward indefinitely, so that it has a fundamentally different lensing effect than the PJ perturber outside of the truncation radius of the PJ perturber. We discuss this in more detail in the Appendix. Another interesting feature is that the shallower NFW profile is not restricted by the position of the lens critical curves in the way the SIS and PJ perturbers are. This shallower profile requires the NFW perturber to have a much larger total mass in order to have the same aperture mass and therefore lensing effect. This limits the NFW to be closer to image A than the other two profiles.

In Figure 6, we plot the marginalised posterior proba-

bility distribution for the perturber mass within 600 pc, assuming that the perturber is located in the plane of the lens galaxy. The 68% confidence intervals for the logarithm of the perturber mass within 600 pc are  $8.2^{+0.6}_{-0.8}$ ,  $8.2^{+0.6}_{-1}$  and  $7.6^{+0.3}_{-0.3}$   $\log_{10}[M_{\text{sub}}/M_{\odot}]$ , for a singular isothermal sphere, PJ, and NFW mass profile respectively. The PJ perturber can occupy lower masses relative to the SIS mass profile due to the truncation radius which simulates tidal stripping, while the NFW profile is restricted to a small range of masses due to its shallow density profile which gives it an effectively weaker lensing signal.

Given the significantly different lensing effects in the three cases, it will be possible with a larger sample of lenses to learn about both the typical mass profile as well as the mass function of the perturbers.

## 7 DISCUSSION

We demonstrate that strongly lensed narrow-line emission provides an alternative to radio emission in lensed quasars for detecting substructure, yielding lens model constraints with consistent results and comparable accuracy. This is important as many more quasars have significant narrow-line emission than radio emission, thus this method can be extended to study substructure in a larger sample of systems. There is significant future potential for this method as ongoing and planned optical surveys such as DES, LSST, PANSTARRS and GAIA are expected to find thousands more lensed quasars based on their optical rather than radio properties (Oguri & Marshall 2010). The next generation of adaptive optics systems (NGAO), (Max et al. 2008), and telescopes such as the Thirty Meter Telescope and the European Extremely Large Telescope will make it possible to measure narrow-line lensing rapidly and with high precision for those large samples of objects. In the nearer future, technology upgrades to the Keck AO system which allow for PSF telemetry will allow for a more accurate characterisation of the PSF, which will allow better constraints on the source size, and thus stronger lower limits on a perturber mass.

In this work we focused on performing a lens model with a single perturbing subhalo to compare our results with previous studies which used radio emission. In the future, it is important to extend this analysis to a larger number of systems, in order to gain a statistical understanding of the subhalo population (Fadely & Keeton 2012).

Significant information is also contained in deep imaging of the lensed systems, which can sometimes reveal luminous substructure (McKean et al. 2007; MacLeod et al. 2009). If a luminous satellite is detected, it can be used to break the degeneracy between the subhalo mass and position, as well as providing a measurement of the subhalo mass to light ratio.

## 8 SUMMARY

We used OSIRIS at Keck with adaptive optics in order to obtain spatially resolved spectroscopy of the gravitational lens B1422+231. We developed a new pipeline which enabled us to robustly extract lensed image spectra, by first

| Model     | host b                    | d Ra                      | d Dec                      | PA                    | $\epsilon$             | $\gamma$                  | $\theta_\gamma$       | $\log_{10}[\text{bSIS}]$ | dRA <sub>SIS</sub>  | dDec <sub>SIS</sub> |
|-----------|---------------------------|---------------------------|----------------------------|-----------------------|------------------------|---------------------------|-----------------------|--------------------------|---------------------|---------------------|
| SIE       | $0.765^{+0.006}_{-0.006}$ | $0.733^{+0.009}_{-0.009}$ | $-0.646^{+0.007}_{-0.007}$ | $-68.8^{+0.3}_{-0.2}$ | $0.21^{+0.02}_{-0.01}$ | $0.217^{+0.006}_{-0.007}$ | $-48.3^{+0.5}_{-0.5}$ | -                        | -                   | -                   |
| SIE + SIS | $0.76^{+0.01}_{-0.02}$    | $0.733^{+0.008}_{-0.008}$ | $-0.650^{+0.007}_{-0.007}$ | $-66^{+3}_{-5}$       | $0.21^{+0.02}_{-0.02}$ | $0.217^{+0.006}_{-0.007}$ | $-48^{+2}_{-2}$       | $-1.9^{+0.6}_{-0.8}$     | $0.5^{+0.1}_{-0.2}$ | $0.4^{+0.2}_{-0.2}$ |

**Table 2.** Posterior median and one sigma confidence intervals for lens model parameters, in the first case assuming the lens is an SIE lens with external shear, and in the second case assuming the lens contains an SIE in external shear and a perturbing subhalo with an SIS mass profile. Results are inferred based on the [OIII] image fluxes and positions. Parameters are defined in Section 5.1. Position angle and shear are in units of degrees East of North while Einstein radii are in units of arcseconds .

| Image | dRa <sub>1</sub>   | dDec <sub>1</sub>  | Flux <sub>1</sub> | dRa <sub>2</sub>  | dDec <sub>2</sub>  | Flux <sub>2</sub> |
|-------|--------------------|--------------------|-------------------|-------------------|--------------------|-------------------|
| A     | $0.382 \pm 0.003$  | $0.313 \pm 0.005$  | $0.775 \pm 0.004$ | $0.387 \pm 0.003$ | $0.315 \pm 0.005$  | $0.88 \pm 0.02$   |
| B     | $0.007 \pm 0.004$  | $0.004 \pm 0.004$  | 1.00              | $0.001 \pm 0.004$ | $0.008 \pm 0.005$  | 1.00              |
| C     | $-0.362 \pm 0.005$ | $-0.735 \pm 0.004$ | $0.464 \pm 0.002$ | $0.361 \pm 0.005$ | $-0.729 \pm 0.004$ | $0.469 \pm 0.007$ |

**Table 3.** Posterior median and 68% confidence interval for model predicted image positions in units of arcseconds and fluxes in the case of a single smooth lens galaxy (1) and a lens galaxy plus perturber with SIS mass profile (2). Results for the other two smooth plus perturber mass profiles are similar.

inferring the PSF and image positions in each exposure. Using this information, we detected a significant deviation from a smooth gravitational lens model, which we used to infer the presence of a perturbing low mass subhalo. Our main results are summarised below:

(i) Using our data reduction pipeline, we were able to measure image positions to 5 mas accuracy and integrated line flux ratios with  $\sim 3\%$  uncertainties.

(ii) The narrow-line flux ratios are consistent with radio measurements, and deviate significantly from the smooth model predictions. The broad-line flux ratios are consistent with the narrow line measurements. Our measurement of the continuum is significantly offset, showing a much stronger deviation from the smooth model, possibly indicative of microlensing in addition to millilensing.

(iii) Based on the narrow-line emission positions and fluxes, we infer position and mass of a single perturbing subhalo assuming three different mass profiles. The mass profile significantly affects possible perturber positions and masses, with an NFW subhalo restricted to the smallest region of parameter space by its shallower mass profile which has a relatively weaker lensing signal. The 68% confidence intervals for the logarithmic perturber mass within 600 pc are:  $8.2^{+0.6}_{-0.8}$ ,  $8.2^{+0.6}_{-1}$  and  $7.6^{+0.3}_{-0.3} \log_{10}[\text{M}_{\text{sub}}/\text{M}_{\odot}]$ , for a singular isothermal sphere, pseudo-Jaffe, and NFW mass profile respectively.

## ACKNOWLEDGMENTS

We thank C. Keeton, S. Mao, G. Dobler, P. J. Marshall, B. Brewer, V. Bennert, A. Pancoast, S. Suyu and C. Kochanek for useful comments and discussion. We also thank support astronomer S. Dahm and observing assistant T. Stickel. AMN and TT acknowledge support by the NSF through CA-REER award NSF-0642621, and by the Packard Foundation through a Packard Fellowship. AMN acknowledges support from a UCSB Dean’s Fellowship.

## REFERENCES

- Amara, A., Metcalf, R. B., Cox, T. J., & Ostriker, J. P. 2006, MNRAS, 367, 1367
- Bennert, N., Falcke, H., Schulz, H., Wilson, A. S., & Wills, B. J. 2002, ApJL, 574, L105
- Benson, A. J., Frenk, C. S., Lacey, C. G., Baugh, C. M., & Cole, S. 2002, MNRAS, 333, 177
- Boylan-Kolchin, M., Bullock, J. S., & Kaplinghat, M. 2011, MNRAS, 415, L40
- . 2012, MNRAS, 422, 1203
- Bradač, M., Schneider, P., Steinmetz, M., Lombardi, M., King, L. J., & Porcas, R. 2002, A&AP, 388, 373
- Bullock, J. S., Kravtsov, A. V., & Weinberg, D. H. 2000, ApJ, 539, 517
- Carlberg, R. G., Grillmair, C. J., & Hetherington, N. 2012, ApJ, 760, 75
- Chakrabarti, S., & Blitz, L. 2009, MNRAS, 399, L118
- Chiba, M., Minezaki, T., Kashikawa, N., Kataza, H., & Inoue, K. T. 2005, ApJ, 627, 53
- Dalal, N., & Kochanek, C. S. 2002, ApJ, 572, 25
- Dobke, B. M., & King, L. J. 2006, A&AP, 460, 647
- Dobler, G., & Keeton, C. R. 2006, MNRAS, 365, 1243
- Dunkley, J., Spergel, D. N., Komatsu, E., Hinshaw, G., Larson, D., Nolta, M. R., Odegard, N., Page, L., Bennett, C. L., Gold, B., Hill, R. S., Jarosik, N., Weiland, J. L., Halpern, M., Kogut, A., Limon, M., Meyer, S. S., Tucker, G. S., Wollack, E., & Wright, E. L. 2009, ApJ, 701, 1804
- Fadely, R., & Keeton, C. R. 2012, MNRAS, 419, 936
- Foreman-Mackey, D., Hogg, D. W., Lang, D., & Goodman, J. 2013, PASP, 125, 306
- Gavazzi, R., Treu, T., Rhodes, J. D., Koopmans, L. V. E., Bolton, A. S., Burles, S., Massey, R. J., & Moustakas, L. A. 2007, ApJ, 667, 176
- Guerras, E., Mediavilla, E., Jimenez-Vicente, J., Kochanek, C. S., Muñoz, J. A., Falco, E., & Motta, V. 2013, ApJ, 764, 160
- Guo, Q., Cole, S., Eke, V., & Frenk, C. 2011, MNRAS, 417, 1278
- Hayashi, K., & Chiba, M. 2012, ApJ, 755, 145
- Hezaveh, Y., Dalal, N., Holder, G., Kuhlen, M., Marrone, D., Murray, N., & Vieira, J. 2013, ApJ, 767, 9

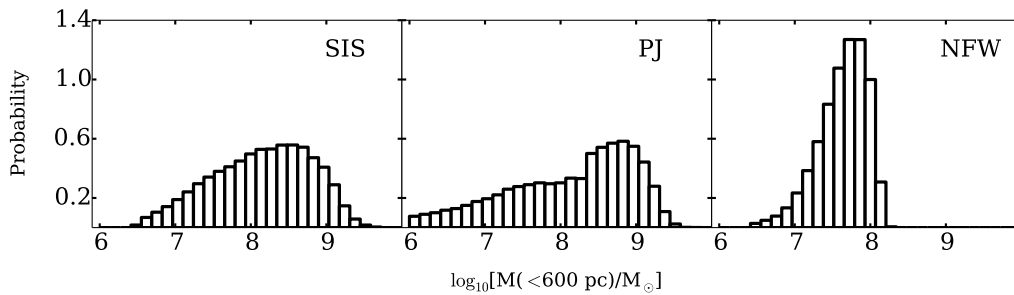


**Figure 6.** Marginalised posterior probability distribution of the perturber mass within 600 pc assuming an SIS, PJ and NFW mass profile respectively from left to right.

- Kaufmann, T., Bullock, J. S., Maller, A., & Fang, T. 2008, in American Institute of Physics Conference Series, Vol. 1035, The Evolution of Galaxies Through the Neutral Hydrogen Window, ed. R. Minchin & E. Momjian, 147–150
- Keeton, C. R. 2001a, ArXiv Astrophysics e-prints
- 2001b, ArXiv Astrophysics e-prints
- 2001c, ArXiv Astrophysics e-prints
- Keeton, C. R., Burles, S., Schechter, P. L., & Wambsganss, J. 2006, *ApJ*, 639, 1
- Keeton, C. R., & Moustakas, L. A. 2009, *ApJ*, 699, 1720
- Klypin, A., Kravtsov, A. V., Valenzuela, O., & Prada, F. 1999, *ApJ*, 522, 82
- Komatsu, E., Smith, K. M., Dunkley, J., Bennett, C. L., Gold, B., Hinshaw, G., Jarosik, N., Larson, D., Nolte, M. R., Page, L., Spergel, D. N., Halpern, M., Hill, R. S., Kogut, A., Limon, M., Meyer, S. S., Odegard, N., Tucker, G. S., Weiland, J. L., Wollack, E., & Wright, E. L. 2011, *ApJS*, 192, 18
- Koopmans, L. V. E. 2005, *MNRAS*, 363, 1136
- Koopmans, L. V. E., Bolton, A., Treu, T., Czoske, O., Auger, M. W., Barnabè, M., Vegetti, S., Gavazzi, R., Moustakas, L. A., & Burles, S. 2009, *ApJL*, 703, L51
- Koposov, S., Belokurov, V., Evans, N. W., Hewett, P. C., Irwin, M. J., Gilmore, G., Zucker, D. B., Rix, H.-W., Fellhauer, M., Bell, E. F., & Glushkova, E. V. 2008, *ApJ*, 686, 279
- Kravtsov, A. V., Berlind, A. A., Wechsler, R. H., Klypin, A. A., Gottlöber, S., Allgood, B., & Primack, J. R. 2004, *ApJ*, 609, 35
- Kundic, T., Hogg, D. W., Blandford, R. D., Cohen, J. G., Lubin, L. M., & Larkin, J. E. 1997, *AJ*, 114, 2276
- Larkin, J., Barczys, M., Krabbe, A., Adkins, S., Aliado, T., Amico, P., Brims, G., Campbell, R., Canfield, J., Gasaway, T., Honey, A., Iserlohe, C., Johnson, C., Kress, E., LaFreniere, D., Magnone, K., Magnone, N., McElwain, M., Moon, J., Quirrenbach, A., Skulason, G., Song, I., Spencer, M., Weiss, J., & Wright, S. 2006, *NAR*, 50, 362
- Lu, Y., Mo, H. J., Katz, N., & Weinberg, M. D. 2012, *MNRAS*, 421, 1779
- Macciò, A. V. 2010, in American Institute of Physics Conference Series, Vol. 1240, American Institute of Physics Conference Series, ed. V. P. Debattista & C. C. Popescu, 355–358
- Macciò, A. V., Dutton, A. A., & van den Bosch, F. C. 2008, *MNRAS*, 391, 1940
- MacLeod, C. L., Kochanek, C. S., & Agol, E. 2009, *ApJ*, 699, 1578
- Mao, S., & Schneider, P. 1998, *MNRAS*, 295, 587
- Max, C., McGrath, E., Gavel, D., Le Mignant, D., Wizinowich, P., & Dekany, R. 2008, in Society of Photo-Optical Instrumentation Engineers (SPIE) Conference Series, Vol. 7015, Society of Photo-Optical Instrumentation Engineers (SPIE) Conference Series
- McKean, J. P., Koopmans, L. V. E., Flack, C. E., Fassnacht, C. D., Thompson, D., Matthews, K., Blandford, R. D., Readhead, A. C. S., & Soifer, B. T. 2007, *MNRAS*, 378, 109
- Menci, N., Fiore, F., & Lamastra, A. 2012, *MNRAS*, 421, 2384
- Metcalf, R. B., & Madau, P. 2001a, *ApJ*, 563, 9
- 2001b, *ApJ*, 563, 9
- Metcalf, R. B., Moustakas, L. A., Bunker, A. J., & Parry, I. R. 2004, *ApJ*, 607, 43
- Moore, B., Ghigna, S., Governato, F., Lake, G., Quinn, T., Stadel, J., & Tozzi, P. 1999, *ApJL*, 524, L19
- Moustakas, L. A., & Metcalf, R. B. 2003, *MNRAS*, 339, 607
- Muñoz, J. A., Kochanek, C. S., & Keeton, C. R. 2001, *ApJ*, 558, 657
- Murayama, T., Taniguchi, Y., Evans, A. S., Sanders, D. B., Hodapp, K.-W., Kawara, K., & Arimoto, N. 1999, *AJ*, 117, 1645
- Navarro, J. F., Frenk, C. S., & White, S. D. M. 1996, *ApJ*, 462, 563
- Nierenberg, A. M., Treu, T., Menci, N., Lu, Y., & Wang, W. 2013, ArXiv e-prints
- Oguri, M., & Marshall, P. J. 2010, *MNRAS*, 405, 2579
- Oke, J. B. 1974, *ApJS*, 27, 21
- Papastergis, E., Martin, A. M., Giovanelli, R., & Haynes, M. P. 2011, *ApJ*, 739, 38
- Patnaik, A. R., Browne, I. W. A., Walsh, D., Chaffee, F. H., & Foltz, C. B. 1992, *MNRAS*, 259, 1P
- Patnaik, A. R., Kembell, A. J., Porcas, R. W., & Garrett, M. A. 1999, *MNRAS*, 307, L1
- Planck Collaboration, Ade, P. A. R., Aghanim, N., Armitage-Caplan, C., Arnaud, M., Ashdown, M., Atrio-Barandela, F., Aumont, J., Baccigalupi, C., Banday, A. J., & et al. 2013, ArXiv e-prints
- Rocha, M., Peter, A. H. G., Bullock, J. S., Kaplinghat, M., Garrison-Kimmel, S., Oñorbe, J., & Moustakas, L. A.

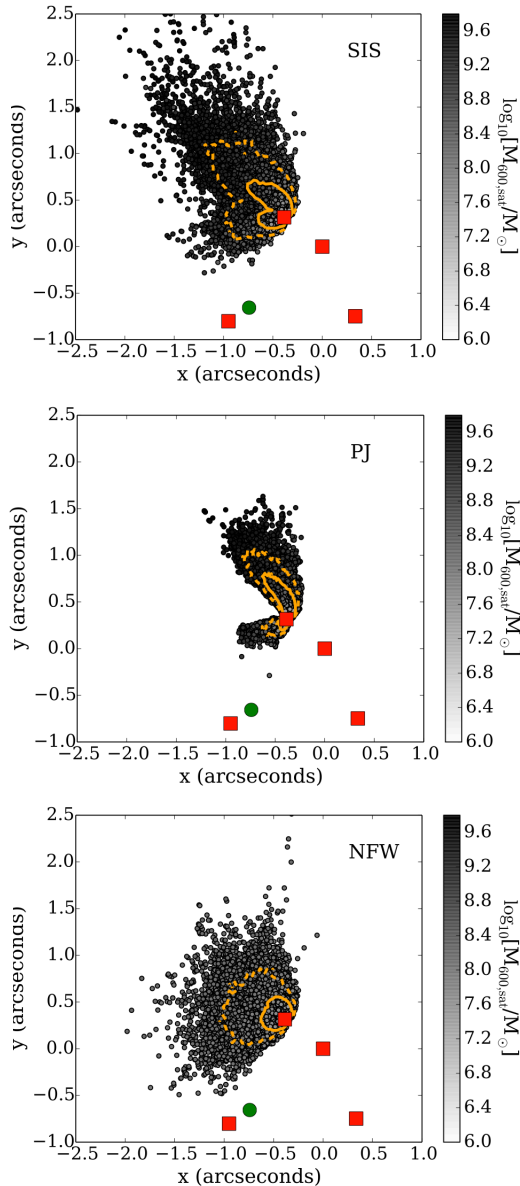


**Figure 5.** Posterior probability distributions of the perturber position relative to the lensed images shown as red squares, and lens galaxy shown as a green circle, for a single SIS, PJ, and NFW perturber from top to bottom. The grey scale represents the perturber mass within 600 pc assuming the perturber is in the plane of the lens galaxy, and solid and dashed contours represent the 68 and 95% confidence contours respectively relative to the most likely position.

- 2013, MNRAS, 430, 81  
 Sluse, D., Chantry, V., Magain, P., Courbin, F., & Meylan, G. 2012a, A&AP, 538, A99  
 Sluse, D., Hutsemékers, D., Courbin, F., Meylan, G., & Wambsganss, J. 2012b, A&AP, 544, A62  
 Somerville, R. S. 2002, ApJL, 572, L23  
 Springel, V. 2010, ARA&A, 48, 391  
 Strigari, L. E., Bullock, J. S., Kaplinghat, M., Diemand, J., Kuhlen, M., & Madau, P. 2007, ApJ, 669, 676  
 Tollerud, E. J., Bullock, J. S., Strigari, L. E., & Willman, B. 2008, ApJ, 688, 277

- Treu, T. 2010, ARA&A, 48, 87  
 van Dam, M. A., Bouchez, A. H., Le Mignant, D., Johansson, E. M., Wizinowich, P. L., Campbell, R. D., Chin, J. C. Y., Hartman, S. K., Lafon, R. E., Stomski, Jr., P. J., & Summers, D. M. 2006, PASP, 118, 310  
 Vegetti, S., Czoske, O., & Koopmans, L. V. E. 2010a, MNRAS, 407, 225  
 Vegetti, S., Koopmans, L. V. E., Bolton, A., Treu, T., & Gavazzi, R. 2010b, MNRAS, 408, 1969  
 Vegetti, S., Lagattuta, D. J., McKean, J. P., Auger, M. W., Fassnacht, C. D., & Koopmans, L. V. E. 2012, Nature, 481, 341  
 Walker, M. G., & Peñarrubia, J. 2011, ApJ, 742, 20  
 Wizinowich, P. L., Le Mignant, D., Bouchez, A. H., Campbell, R. D., Chin, J. C. Y., Contos, A. R., van Dam, M. A., Hartman, S. K., Johansson, E. M., Lafon, R. E., Lewis, H., Stomski, P. J., Summers, D. M., Brown, C. G., Danforth, P. M., Max, C. E., & Pennington, D. M. 2006, PASP, 118, 297  
 Wolf, J., & Bullock, J. S. 2012, ArXiv e-prints  
 Zolotov, A., Brooks, A. M., Willman, B., Governato, F., Pontzen, A., Christensen, C., Dekel, A., Quinn, T., Shen, S., & Wadsley, J. 2012, ApJ, 761, 71

## APPENDIX A: VARIATION IN LENSING EFFECT WITH PERTURBER MASS PROFILE

In this appendix we illustrate the difference in the posterior probability distributions for the perturber position and mass seen in Figure 5 in the case of the PJ and SIS perturber, by means of a simple example. The most notable difference between the two models is the large gap to the East of image A in the case of the PJ perturber. In order to clarify the origin of this difference, in Figure A1 we show the model prediction for the image positions the perturber Einstein radius is varied for fixed position in the case that the perturber is in the gap (position 2), and also in the region further North which is permitted for both mass profiles (position 1). The perturber positions relative to the lensed images are given in the lower left panel of Figure A1.

The first thing to note in this figure is that the perturber in position 1 does not provide a good fit to the observation in either the case of the SIS or PJ perturber (the best fit  $\chi^2$  per degree of freedom is approximately 8 in the case of the SIS perturber, and  $\sim 50$  in the case of the PJ perturber). This figure illustrates the fundamental difference in the lensing effect between the truncated and non-truncated perturber profiles, due to the fact that the lensing signal in the case of the truncated profile is dominated by shear, while the SIS profile has significant convergence at the image position. In position 2, the PJ profile simply cannot provide a good fit to the astrometry, irrespective of its mass.

In Figure A2 we plot the resulting flux ratios as the perturber masses are varied in the two cases. As before, we see that in both cases, the perturber in position 2 provides a less good fit to the observation in the case of the SIS. The fit is much worse though in the case of the PJ perturber. Unlike the case of the SIS profile, in position 2 the flux of image A relative to image B does not increase significantly as the perturber mass is increased for the PJ perturber. As expected, the flux ratio between image B and C does not

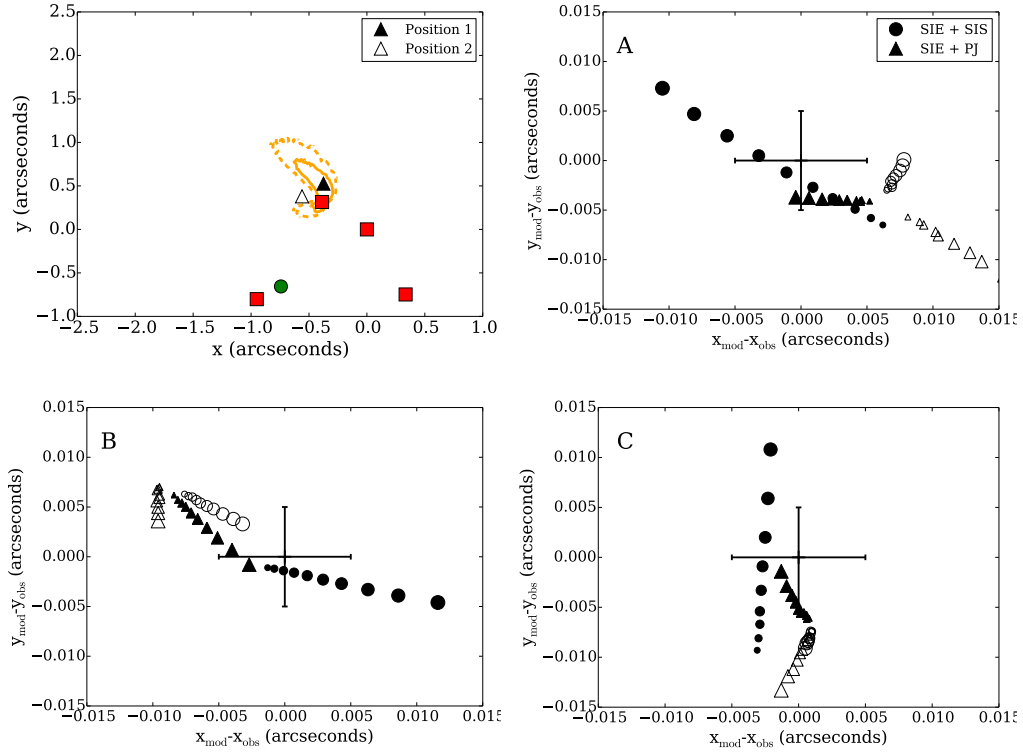


**Figure A1.** Demonstration of how the model image positions vary relative to the observed image positions as the perturber Einstein radius is varied from 0.003 to 0.013 arcseconds logarithmically for fixed perturber position and SIE macromodel parameters, for an SIS and PJ perturber represented by circles and triangles respectively. Point sizes increase with increasing perturber Einstein radius. We explore two perturber positions, illustrated in the upper left panel by open and filled triangles, where the red squares and green circle represent observed image and galaxy positions respectively and the solid and dashed contours represent the 68% and 95% confidence interval for the position of the perturber in the case of the PJ mass profile.

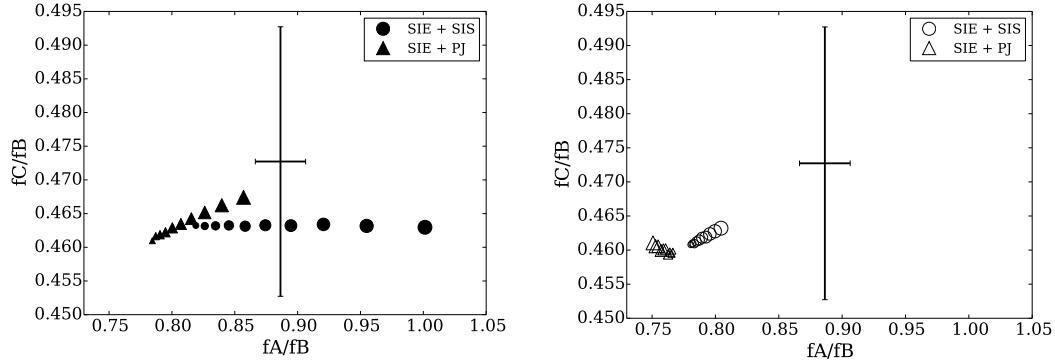


**Figure A2.** Model flux ratios as the perturber mass is varied for fixed position for two different mass profiles in the same way as in Figure A1. For clarity, we show results for positions one and two separately.

vary significantly as the perturber mass is varied, since the dominant effect is to alter the flux of image A.

This paper has been typeset from a  $\text{T}_{\text{E}}\text{X}/\text{L}^{\text{A}}\text{T}_{\text{E}}\text{X}$  file prepared by the author.